Nano-Micro Letters

e-ISSN 2150-5551
CN 31-2103/TB

ARTICLE

https://doi.org/10.1007/s40820-025-01701-8

Cite as
Nano-Micro Lett.
(2025) 17:200

Received: 17 November 2024
Accepted: 18 February 2025

Catalysis-Induced Highly-Stable Interface on Porous Silicon for High-Rate Lithium-Ion Batteries

Zhuobin Han[1], Phornphimon Maitarad[1,8], Nuttapon Yodsin[2], Baogang Zhao[1], Haoyu Ma[1], Kexin Liu[1], Yongfeng Hu[3], Siriporn Jungsuttiwong[4], Yumei Wang[5], Li Lu[5], Liyi Shi[1,7], Shuai Yuan[1], Yongyao Xia[6] ✉, Yingying Lv[1] ✉

HIGHLIGHTS

- In situ etching and co-growth of ultra thin defect-rich oxide layers on porous silicon.
- Through the construction of nano-sized catalytic interface, the electrolyte addition FEC would decompose to a LiF-rich solid electrolyte interphase (SEI).
- The robust SEI on porous structured silicon performs high-rate stability at varied temperatures.

ABSTRACT Silicon stands as a key anode material in lithium-ion battery ascribing to its high energy density. Nevertheless, the poor rate performance and limited cycling life remain unresolved through conventional approaches that involve carbon composites or nanostructures, primarily due to the un-controllable effects arising from the substantial formation of a solid electrolyte interphase (SEI) during the cycling. Here, an ultra-thin and homogeneous Ti doping alumina oxide catalytic interface is meticulously applied on the porous Si through a synergistic etching and hydrolysis process. This defect-rich oxide interface promotes a selective adsorption of fluoroethylene carbonate, leading to a catalytic reaction that can be aptly described as "molecular concentration-in situ conversion". The resultant inorganic-rich SEI layer is electrochemical stable and favors ion-transport, particularly at high-rate cycling and high temperature. The robustly shielded porous Si, with a large surface area, achieves a high initial Coulombic efficiency of 84.7% and delivers exceptional high-rate performance at 25 A g^{-1} (692 mAh g^{-1}) and a high Coulombic efficiency of 99.7% over 1000 cycles. The robust SEI constructed through a precious catalytic layer promises significant advantages for the fast development of silicon-based anode in fast-charging batteries.

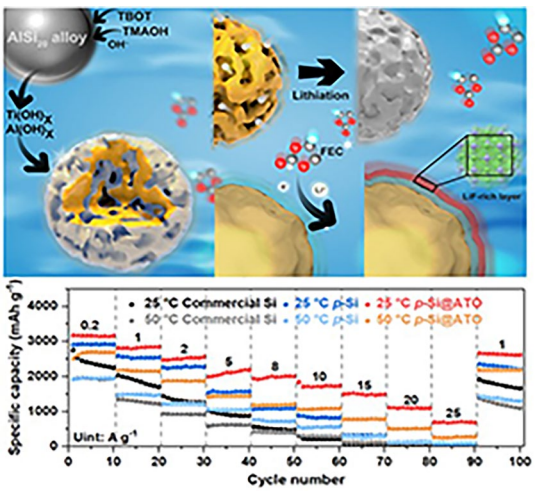

KEYWORDS Catalytic interface; Mesoporous; Inorganic-rich SEI; Silicon anode; Lithium-ion batteries

Zhuobin Han and Phornphimon Maitarad have contributed equally to this work.
✉ Yongyao Xia, yyxia@fudan.edu.cn; Yingying Lv, yyinglv@shu.edu.cn
[1] Research Centre of Nanoscience and Nanotechnology, Shanghai University, Shanghai 200444, People's Republic of China
[2] Department of Chemistry, Faculty of Science, Silpakorn University, Nakhon Pathom 73000, Thailand
[3] Sinopec Shanghai Research Institute of Petrochemical Technology Co., Ltd., Shanghai 201208, People's Republic of China
[4] Department of Chemistry and Center of Excellence for Innovation in Chemistry Faculty of Science, Ubon Ratchathani University, Ubon Ratchathani 34190, Thailand
[5] National University of Singapore (Chongqing) Research Institute, Chongqing 401123, People's Republic of China
[6] Department of Chemistry, Fudan University, Shanghai 200433, People's Republic of China
[7] Emerging Industries Institute Shanghai University, Jiaxing 314006, Zhejiang, People's Republic of China
[8] Program in Bioinformatics and Computational Biology, Graduate School, Chulalongkorn University, Bangkok 10330, Thailand

Published online: 26 March 2025

Shanghai Jiao Tong University Press

Springer

1 Introduction

Silicon anodes, with high theoretical specific capacity of 3579 mAh g^{-1} hold a predominate position in the commercial market for high energy density lithium-ion batteries. However, huge volume change of Si (~300%) during lithiation/delithiation, always leads to capacity degradation [1, 2], demonstrating low power density and limited cycling life, especially at high temperature. On the interface of silicon, the solid electrolyte interphase (SEI) is fragile and unstable, which could not sustain the huge volume change of the silicon, would be continuous destroyed and re-formation at the repeating cycles [3, 4].

Nano-structured Si is developed to improve the ion transportation at high current density, for example, nanoparticle, nanowire, porous structure or composites. Although structural stability is improved, severe chemical reactions at the interface cannot be fully addressed through the above strategy. The large specific surface area of nanostructures and repeating side reaction would consume the electrolyte, lead to fast capacity degradation [1, 5]. The adverse reactions would accelerate at high temperatures, might precipitate thermal runaway, posing significant safety risks [6, 7]. In essence, designing the stable SEI with specific composition and structure could be achieved through electrolyte modulation and electrode design. However, devising an efficacious interfacial protection layer between the electrode and electrolyte is a critical challenge.

Recently, the interaction between electrodes and electrolytes have gathered increasing attention [8–11]. The deployment of high-concentration or localized high-concentration electrolytes can modulate the solvation structure of lithium ions, thereby engendering a stable SEI [12, 13]. Meanwhile, the incorporation of electrolyte additives to improve the interfacial stability of the electrode, such as vinylene carbonate (VC) and fluoroethylene carbonate (FEC) have been shown [14–16]. FEC, in particular, is widely used due to its higher reduction potential compared with other electrolyte components [17–19], which is decomposed to form a stable LiF-rich SEI. LiF is considered as a key inorganic component of SEI, owing to its high chemical stability and electronic insulating [20]. Most of the research is focused on the formation of an SEI with specific components through electrolyte modulation, while the establishment of a robust SEI layer on anode materials through a surface engineering strategy is rarely studied.

The redox of the electrolyte have diverse pathways and lead to varied reactivity during the presence of varied interface. Meanwhile, transition metals with special d-orbitals are conjectured to catalyze the electrolyte's decomposition [21, 22]. Furthermore, the introduction of surface defects can effectively improve the electrochemical activity by modulating functional groups or incorporating heteroatoms [23–25]. It is widely acknowledged that adsorption is prior to catalysis. Thus, through the deliberate design of electrode structures and electrolyte compositions, targeted solvent molecules can be specifically adsorbed onto the inner Helmholtz plane (IHP) of the electric double layer at the electrode surface. Subsequently, solvent molecules in IHP are preferentially decomposed to form the SEI with specific composition [26, 27]. Thus, a catalytic process achieved through precise synthetic control of the electrode is urgently required, and a robust SEI can be realized.

Therefore, how to solve these problems simultaneously is a major challenge. Through a spontaneous in situ etching and co-growth process, an amorphous alumina-titanium oxide layer is coated on the surface of as-formed porous Si. As prospect, a preferential adsorption of FEC, together with the catalytic effect from defect-rich oxide layer, would generate an inorganic LiF-rich SEI through a fasten-catalytic process. More importantly, from room temperature to high temperature, the LiF-rich interface perform excellent cycling stability (capacity retention is 79.8% after 1000 cycles at 5 A g^{-1}), high-rate performance (the capacity reaches 692 mAh g^{-1} even at 25 A g^{-1}) and high temperature stability (capacity retention is 80.0% after 500 cycles at 50 °C). This comprehensive understanding of the interface dynamics and catalytic reaction-induced robust SEI processes is vital for the ongoing development and optimization of anode materials for high-performance lithium-ion batteries at high temperature.

2 Experimental Section

2.1 Materials Preparation

2.1.1 Synthesis of p-Si@ATO

Typically, 0.2 g of commercial $AlSi_{20}$ alloy (Changsha Tianjiu metal material Co., China) is dispersed in 100 mL of ethanol, then 1.6 g of tetramethylammonium hydroxide (TMAOH, dissolved in 1 mL of water) that provides an

https://doi.org/10.1007/s40820-025-01701-8

alkaline environment and 15 mg of tetrabutyl orthotitanate (TBOT) were added sequentially to the above solution. After stirring at 60 °C for 12 h, 1.6 g of TMAOH was added and stirred for another 12 h. The resulting product was centrifuged with ethanol for three times and dried overnight at 80 °C under vacuum. The obtained powder was dispersed into 0.1 M HCl etched 24 h to remove residual Al. Then washed with deionized water to neutral, finally, centrifuged with ethanol and dried at 80 °C under vacuum.

2.1.2 Synthesis of p-Si

1.0 g of commercial $AlSi_{20}$ alloy was dispersed into 0.1 M HCl etched 24 h to remove Al. Then, washed with water to neutral, finally, centrifuged with ethanol three times and dried overnight at 80 °C under vacuum. (Because Si is not tolerant of strong alkaline environments and it is difficult to fully etch metal Al while also producing a thick layer of alumina, we have opted for acidic etching conditions instead.)

2.2 Material Characterizations

The morphology and microstructure were characterized by field-emission scanning electron microscopy (FESEM, JSM-7500, JEOL) and transmission electron microscopy (TEM, JEM-2100Plus, JEOL). The crystal structure and chemical bonds of materials were characterized by X-ray diffraction (XRD, SmartLab) with Cu K_α radiation ($\lambda = 0.154$ nm), X-ray photoelectron spectroscopy (XPS, Kratos AXIS SUPRA$^+$, Shimadzu) equipped with Al K_α radiation, and the binding energy was calibrated by the C 1*s* peak (284.8 eV) of contamination carbon. Nitrogen sorption/desorption isotherms were tested at 77 K with the Autosorb-IQ2 (Quantachrome Corporation), the specific surface area (SSA) is measured via BET method and the distribution of pore size is determined using density functional theory (DFT) method. Oxygen vacancies and electron paramagnetism are characterized by electron paramagnetic resonance (EPR) with Bruker A300 at 25 °C. Diffuse reflectance infrared Fourier transform spectroscopy (DRIFTS) of pyridine adsorption is carried out on a Nicolet iS50 spectrometer (Thermo Fisher, USA). The *p*-Si@ATO powder was pretreated under He flow (30 mL min^{-1}) at 150 °C for 1 h, the system was cooled down to 25 °C, then the background was collected. Pyridine was injected into the system for 30 min followed by He purging (30 mL min^{-1}) for 30 min to remove weakly adsorbed pyridine. Finally, Pyridine adsorption infrared (IR) spectrum was collected at 25 °C. The X-ray absorption spectroscopy (XAS) experiments of *p*-Si@ATO powder were conducted at the Ti *K*-edge on BL14W1 at Shanghai Synchrotron Radiation Facility. Data were acquired in fluorescence mode at room temperature.

2.3 Cell Assembly and Electrochemical Measurements

The working electrode slurry was fabricated by mixing 80 wt% active materials, 10 wt% polyacrylic acid (PAA, average $M_n = 450{,}000$, Sigma-Aldrich), and 10 wt% acetylene black in N-methyl-2-pyrrolidone (99.9%, Sigma-Aldrich). The as-received slurry was coated on Cu foil and then dried at 80 °C overnight in a vacuum oven. Unless otherwise specified, the loading of the active material was approximately 0.7–1.8 mg cm^{-2}. The stainless-steel coin cell (CR2032, Kejing Co., Ltd.) was assembled inside an argon-filled glovebox (O_2 and H_2O content < 0.1 ppm) with the synthesized material and lithium foil as counter electrode. In all tests, 1.0 M $LiPF_6$ dissolved in ethylene carbonate (EC) and diethyl carbonate (DEC) (1:1 volume ratio) with 15% FEC as electrolyte and Celgard 2500 film as separator were used. All cells were rested 24 h before cycle. The cycling and rate performance were evaluated by galvanostatic charge/discharge measurements conducted on the LAND CT3002A (Wuhan LAND electronics Co., Ltd., China) testing system between 0.01 and 2.0 V (versus Li$^+$/Li) at 25/50 °C. For high temperature cycling, the cell is activated two cycles at 0.2, 0.5, 1, and 2 A g^{-1}, respectively. For high-rate cycling, the cell is activated two cycles at 0.2, 0.5, 1, 2, 5, 8, 10, and 15 A g^{-1}, respectively. For pouch cell, the active material loading of anode is 0.5 mg cm^{-2}, $LiFePO_4$ is 10.2 mg cm^{-2}, N/P≈0.85. The voltage range is 2.5–3.9 V, and 1 C = 160 mAh g^{-1}. Neither the anode nor cathode electrodes are pre-lithiated.

Electrochemical impedance spectroscopy (EIS) with a frequency range of 1.0 M–0.01 Hz and a voltage amplitude of 5.0 mV were conducted on Gamry Reference 600+. For in situ EIS, EIS data is collected at different voltages, during

the discharge/charge process at 0.2 A g^{-1}. The obtained EIS data were analyzed by distribution of relaxation times (DRT) after satisfying the Kramers-Kronig relationship. Nyquist diagrams typically necessitate equivalent circuit models for the analysis of electrochemical processes. This presents a significant challenge in accurately distinguishing individual electrochemical reactions amid multifaceted interface interactions. DRT analysis enables the direct determination of the time constants (τ) associated with the primary electrochemical processes, thereby streamlining impedance analysis and notably enhancing the precision of kinetic interpretations concerning time scales. The DRT describes the time relaxation characteristics of the electrochemical system analyzed, isolates the processes with different time constants, and it gives direct access to the distribution of the timescales. During the actual measurement, there is noise interference, in situ EIS and DRT results are only used to show the trends of each process as a semiquantitative method instead of using it as quantitative method. We used the open MATLAB code shared online by Prof. Francesco Ciucci (https://github.com/ciuccislab/DRTtools).

2.4 Theoretical Simulations

All calculations were performed based on the DFT-D3, as implemented in Vienna ab initio simulation package (VASP). The generalized gradient approximation (GGA) with Perdew-Burke-Ernzerhof (PBE) functional was used to describe the electron exchange–correlation. In this case, a supercell of size $3\times3\times1$ was used to simulate Li adsorption. The vacuum spacing along the z-axis was 15 Å to avoid the interaction between the layer and its periodically repeated images. With a cutoff energy of 450 eV, the structures relaxation has no any symmetry constraints. The convergence threshold for energy was set to 1×10^{-5} eV and the force was chosen as 0.02 eV $Å^{-1}$. The k-points were set as gamma 111.

3 Results and Discussion

3.1 Structure of Defect-Rich Oxides Layer

The $AlSi_{20}$ microsphere with a particle size approximately 1.2 μm (Fig. S1) are used as initial material directly.

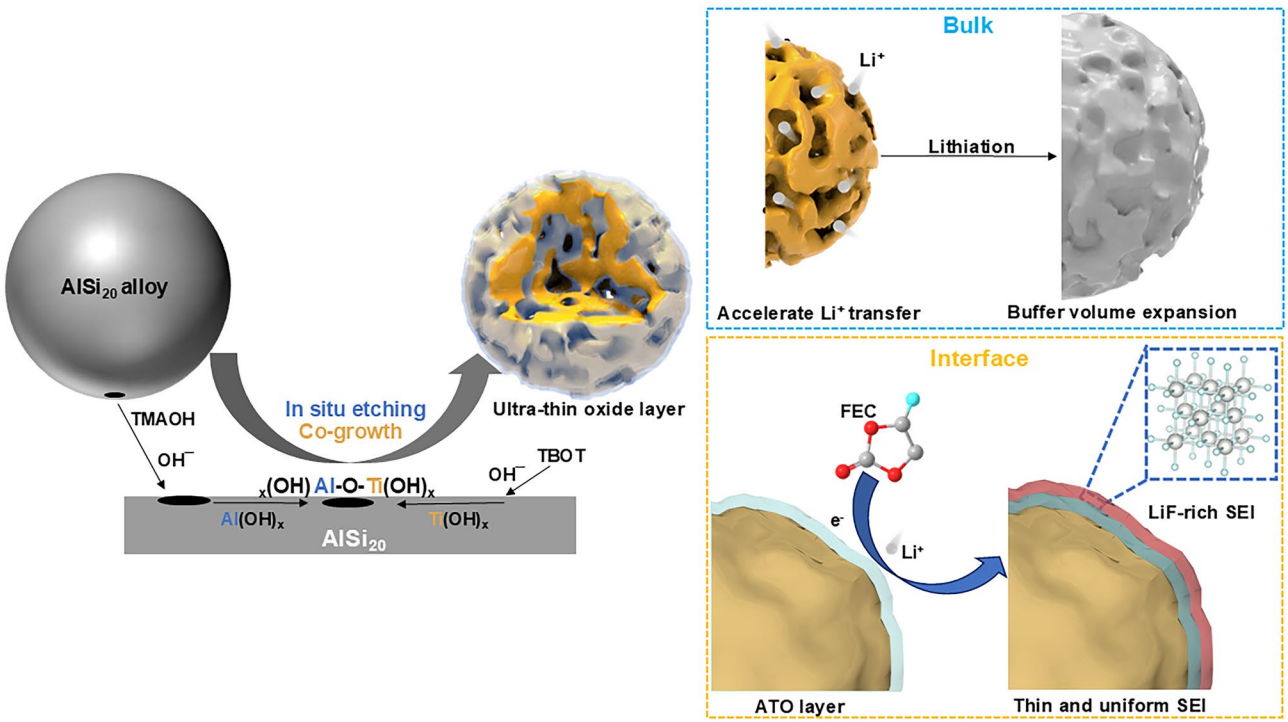

Fig. 1 Schematic illustration of the in situ etching and co-growth procedures for *p*-Si@ATO and the corresponding porous structure and surface property

https://doi.org/10.1007/s40820-025-01701-8

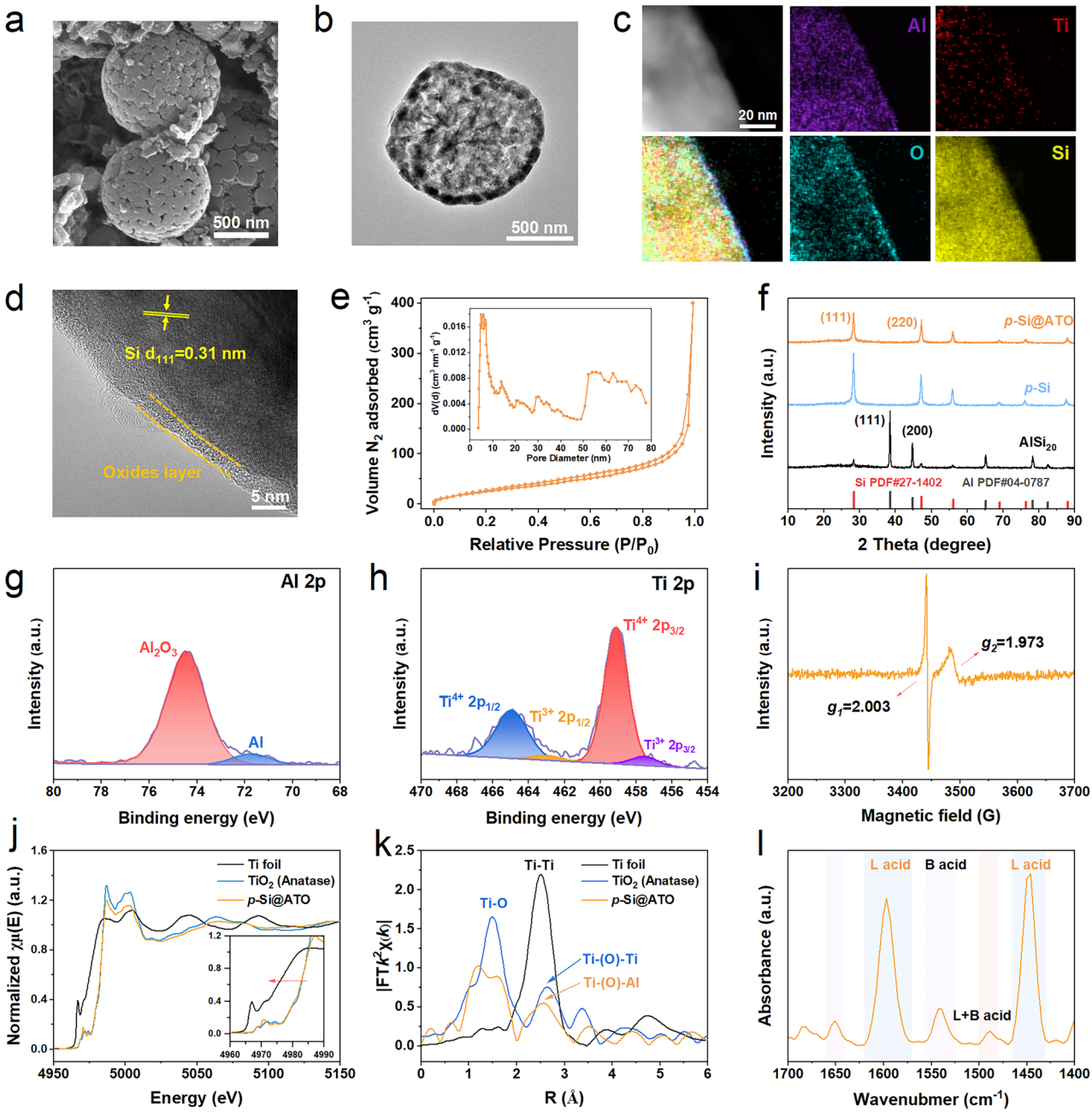

Fig. 2 Structural characterizations of *p*-Si@ATO. **a** SEM image of *p*-Si@ATO particle. **b** TEM image of *p*-Si@ATO particle. **c, d** Elemental mapping images and HRTEM image of surface oxides layer. **e** Nitrogen sorption/desorption isotherms and the corresponding pore size distribution of *p*-Si@ATO. **f** XRD pattern of *p*-Si@ATO, *p*-Si and $AlSi_{20}$ alloy. **g, h** High-resolution Al 2*p* and Ti 2*p* XPS of *p*-Si@ATO. **i** EPR spectroscopy of *p*-Si@ATO powder at 25 °C. **j** Normalized Ti *K*-edge XAS spectra of Ti foil, TiO_2 and *p*-Si@ATO. **k** Fourier transform of EXAFS R-space in k^2-weighted. **l** Pyridine IR spectroscopy of *p*-Si@ATO powder at 25 °C

Through a controlled in situ etching and co-growth process in an alkaline environment, the mild etching and simultaneous oxidation of aluminum occur on the surface of the alloy microsphere, in conjunction with hydrolysis of trace amount of TBOT. Thus, porous Si with a homogeneous alumina and titanium oxide layer (referred to as *p*-Si@ATO) can be obtained (Fig. 1). This intricate interplay of etching and hydrolysis coupled with subsequent dehydration culminates in the etching of aluminum and the formation of alumina-titanium oxide layer on the porous Si. Pure porous Si (denoted as *p*-Si) is obtained after the etching of aluminum using the same alloy microspheres.

The as-synthesized *p*-Si@ATO (Fig. 2a) retains the spherical morphology characteristic of the $AlSi_{20}$ alloy, with the surface revealing open pores on the order of tens of nanometers. TEM image (Figs. 2b and S4) displays the unique hollow, dendritic porous architecture of the *p*-Si@ATO. The nitrogen sorption–desorption isotherms (Fig. 2e) exhibit a type IV isotherm [28]. The *p*-Si@ATO reveals a surface area of 112.4 $m^2\ g^{-1}$. The pore size distribution is bimodal, featuring a mesopore diameter centered at about 4.9 nm and a macropore range spanning 50–80 nm. These pores should be raised from the selective etching of aluminum, serving to accommodate the volumetric expansion of Si and enhancing mass transfer rates. The specific surface areas of *p*-Si and commercial Si are 98.5 and 10.1 $m^2\ g^{-1}$, respectively (Figs. S5 and S6). High-resolution TEM (HRTEM) images (Fig. 2c, d) show that the *p*-Si@ATO microsphere is enveloped by a homogeneous amorphous shell approximately 3–5 nm thick which has the Ti, Al and Si elements in the oxide layer on the surface. The presence of distinct lattice fringes with a spacing of 0.31 nm correlates to the (111) crystal plane of Si [29]. The disappearance of the metallic Al peak in the XRD pattern (Fig. 2f) after etching suggests that the metallic Al has been removed from the *p*-Si and *p*-Si@ATO material. Inductively coupled plasma-atomic emission spectrometry analysis quantifies the composition of the *p*-Si@ATO as approximately 85 wt% Si, 5 wt% Al and 0.3 wt% Ti (Table S1).

3.2 Surface Chemical Environment

XPS corroborates the presence of an oxide layer. The natural silicon oxide layer is present on the surfaces of *p*-Si@ATO, *p*-Si and commercial Si (Figs. S9d, f and S10). The Al 2*p* spectra (Fig. 2g) exhibit not only the expected Al_2O_3 peak at 74.4 eV but also a minor peak at 71.7 eV, indicating that the metallic Al may contribute partial lithium storage capacity and enhance the internal electronic conductivity. The Ti 2*p* spectrum (Fig. 2h) presents two pronounced peaks at 459.0 and 464.7 eV, corresponding to the $2p_{3/2}$ and $2p_{1/2}$ of Ti^{4+}, respectively. Intriguingly, subordinate peaks at 457.2 and 463.1 eV suggest the existence of Ti^{3+} [30]. EPR spectroscopy (Fig. 2i) at 25 °C reveals two distinct paramagnetic signals at $g_1 = 2.003$ and $g_2 = 1.973$, ascribed to oxygen vacancies and Ti^{3+}, respectively [30, 31]. The presence of Ti^{3+} and oxygen vacancies is acknowledged for their capacity to significantly enhance electronic conductivity and the adsorption of negative charges [31, 32]. Moreover, these oxygen vacancies are instrumental in enhancing the charge transport capabilities of semiconductor electrocatalysts by facilitating the excitation of delocalized electrons to the conduction band, thereby increasing charge carrier density [33].

To decipher the formation of Ti^{3+}, the same coating strategy is employed using commercially pure Si instead of the $AlSi_{20}$ alloy for comparative analysis. Unexpectedly, the EPR spectrum (Fig. S11) only identifies oxygen vacancies at $g = 2.002$ with the conspicuous absence of Ti^{3+} signal. Under alkaline conditions, the etching of metallic Al and the hydrolysis of TBOT yield the formation of hydroxides. During the ensuing in situ co-growth phase, these hydroxides are presumed to interlink via Al-O-Ti bonds, forming an ultra-thin amorphous oxide layer. Given the extremely low Ti content (~0.3 wt%), synchrotron XAS in fluorescence mode is performed on the *p*-Si@ATO powder to probe the Al-O-Ti bonds and the precise chemical environment of Ti. The Ti *K*-edge spectrum (Fig. 2j) reveals that the edge energy of *p*-Si@ATO is similar to that of TiO_2 (anatase), but with a small shift to lower energy and lower peak area, signifying a somewhat reduced valence state of Ti in *p*-Si@ATO straddles in comparison to TiO_2. This aligns with the Ti^{3+} presence inferred from EPR. The Fourier-transformed extended X-ray absorption fine structure (EXAFS) oscillations (Fig. 2k) delineate the radial distribution of neighboring atoms around the Ti atom, with the peak at approximately 1.5 Å representing the characteristic Ti-O bond [34, 35]. And the intensities of both Ti-O peak and higher order feature (around 2.5 Å) are much reduced compared to those of Ti reference, suggesting a smaller coordination number in *p*-Si@ATO. Meanwhile, *p*-Si@ATO the shift to a smaller R

 https://doi.org/10.1007/s40820-025-01701-8

at 2.5 Å, since Al has a smaller radius than Ti, this implies the presence of the Al-O-Ti bond.

The pyridine IR is utilized to investigate the acidic sites on the *p*-Si@ATO surface (Fig. 2l). The distinct absorption bands at 1596.8 and 1446.4 cm^{-1} denote the existence of Lewis (L) acid sites, while the weaker bands at 1542.8 cm^{-1} imply the presence of trace Brønsted (B) acid sites. Additionally, the absorbance near 1488.8 cm^{-1} is indicative of both L and B acid sites on the *p*-Si@ATO surface [36, 37]. Al_2O_3, a potent Lewis acid, is extensively applied in catalysis, and it has been proved that the formation of Al-O-Ti bond can enhance its Lewis acidity due to create a greater number of coordinatively unsaturated metal sites [36, 38]. These Lewis acid sites facilitate the adsorption of negative charges, and the establishment of Al-O-Ti bonds on the *p*-Si@ATO surface aids in adsorbing the electrolyte and catalyzing its decomposition. In summation, the surface of porous Si is coated with a 3–5 nm amorphous oxide layer via an in situ etching and co-growth strategy, validating the existence of Al-O-Ti bond. The plentiful Lewis acid sites on the surface favor electrolyte adsorption, while the presence of Ti^{3+} and oxygen vacancies enhance electronic conductivity. These surface characteristics are favorable for the adsorption and mass transfer of the electrolyte in *p*-Si@ATO, thereby engendering a stable SEI. Meanwhile, the abundant mesopore can improve the adsorption of the electrolyte, accelerate the mass transfer rate and buffer the volume expansion.

3.3 Electrochemical Performance

The porous structure offers abundant internal space to accommodate the significant volume changes of Si during lithiation/delithiation. However, the repeated growth of the SEI and the resultant consumption of electrolyte are inevitable problems. To assess the impact of the porous structure and the surface functionality of the ATO layer, detailed electrochemical analyses are conducted on *p*-Si@ATO and commercial Si electrodes. The initial Coulombic efficiency (ICE) of commercial Si is only 79.2% at 25 °C and 70.2% at 50 °C, while the ICE of *p*-Si@ATO at 0.2 A g^{-1} is as high as 84.7% at 25 °C and 73.2% at 50 °C, markedly surpassing the ICE of commercial Si. Notably, pure *p*-Si exhibits lowest ICE, which is only 71.6% at 25 °C and 61.3% at 50 °C, might be due to its extensive specific surface area and lack of effective interface protection (Fig. S14). The improvement in ICE with *p*-Si@ATO is attributed to enhanced interface protection effect of the oxide layer, which reduces side reactions compared to the unstable surface of commercial Si. Furthermore, the initial charge capacity of *p*-Si@ATO (3312 mAh g^{-1} at 25 °C and 2423 mAh g^{-1} at 50 °C) exceeds that of the *p*-Si (2985 mAh g^{-1} at 25 °C and 1987 mAh g^{-1} at 50 °C) and commercial Si (2910 mAh g^{-1} at 25 °C and 1893 mAh g^{-1} at 50 °C). The capacity of the *p*-Si@ATO, *p*-Si and commercial Si at 50 °C is significantly lower than that at room temperature, with rapid capacity degradation at elevated temperatures being attributed to the instability of $LiPF_6$-based electrolytes, besides, the interfacial side reactions are more serious at high temperatures, resulting in lower Coulombic efficiency than that at room temperature [39, 40].

At 25 °C (Fig. 3a), after 1000 cycles at 5 A g^{-1}, the capacity retention of the commercial Si is only 13.7% (based on the third cycle) and *p*-Si is 41.1%, whereas *p*-Si@ATO demonstrates exceptional capacity retention of 79.8%, which has the average CE of about 99.7% over these 1000 cycles. After 500 cycles at 2 A g^{-1} (Fig. S15), the capacity retention of *p*-Si@ATO is 99.5% which is significantly higher than *p*-Si and commercial Si. At 50 °C (Fig. 3b), the capacity retention of the commercial Si plummets to 42.9% after 100 cycles and *p*-Si to 44.9% after 500 cycles at 5 A g^{-1}. In stark contrast, *p*-Si@ATO maintains 67.5% capacity after 500 cycles at 5 A g^{-1}. Meanwhile, *p*-Si@ATO maintains 80.0% capacity after 500 cycles at 2 A g^{-1}, with average CE around 98.9% (Fig. S16). Furthermore, the rate performance of *p*-Si@ATO is also evaluated at varied of current densities from 0.2 to 25 A g^{-1} (Fig. 3c). At high current densities of 10, 15 and 20 A g^{-1}, the capacities are 1730, 1492, and 1103 mAh g^{-1} at 25 °C, respectively. At 50 °C, they are 1076, 784, and 512 mAh g^{-1}. Remarkably, even at an extremely high current density of 25 A g^{-1}, *p*-Si@ATO maintains a considerable reversible capacity (692 mAh g^{-1} at 25 °C and 270 mAh g^{-1} at 50 °C), whereas the capacity of the *p*-Si and commercial Si drops down to near zero at 20 A g^{-1}. The porous structure enables rate performance of *p*-Si@ATO and *p*-Si better than commercial Si, besides, *p*-Si@ATOs with interface protection has best rate performance and capacity. The *p*-Si@ATO electrode also demonstrates excellent high-rate cycling stability, maintaining steady cycling performance over 1000 cycles at 10, 15, and 20 A g^{-1} at 25 °C (Fig. 3d). Such a high reversible capacity, high-rate capability, durable

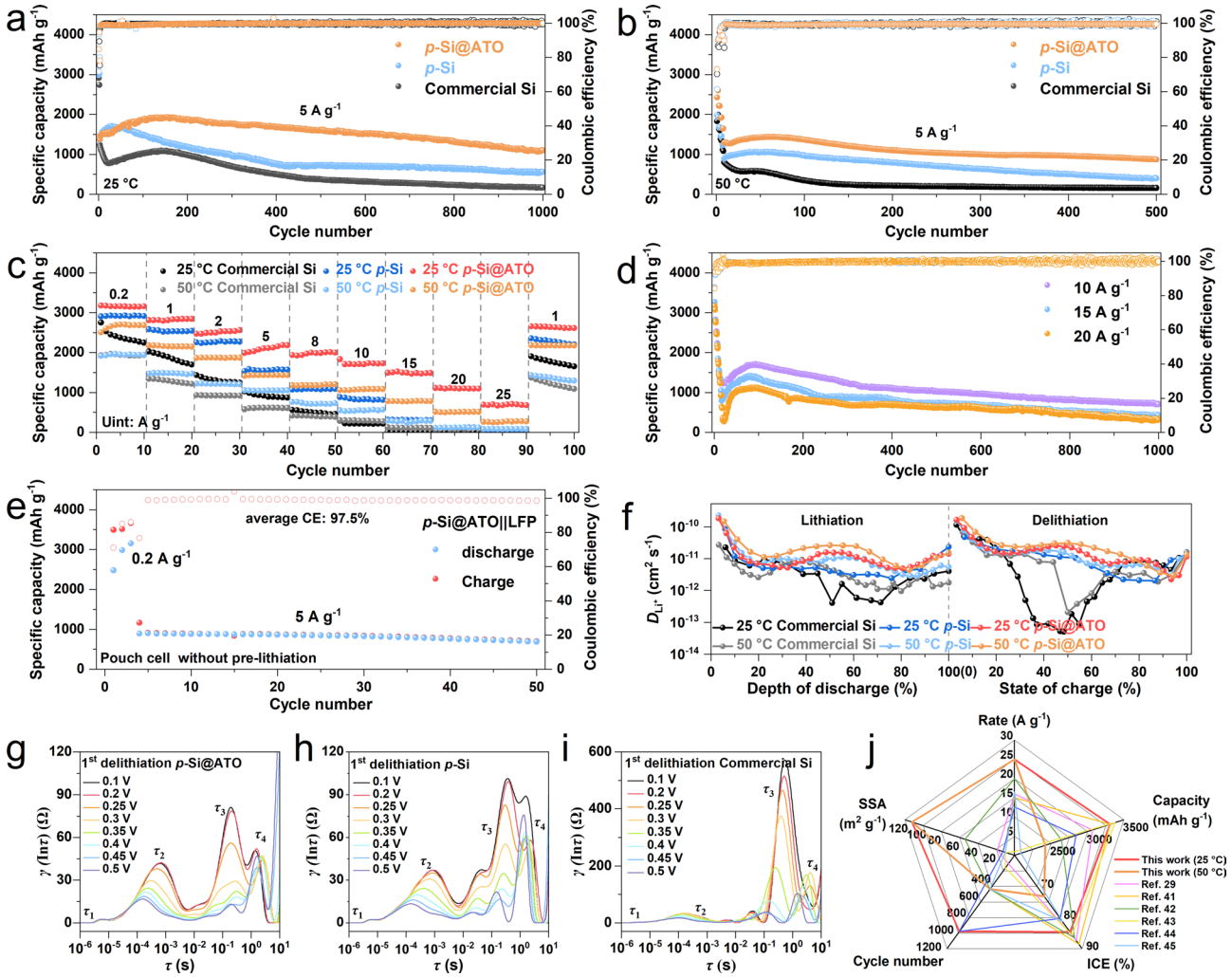

Fig. 3 Electrochemical performance of *p*-Si@ATO, *p*-Si and commercial Si anode. **a, b** Long-term cycling performances of *p*-Si@ATO, *p*-Si and commercial Si at 25 and 50 °C. **c** Rate performances of *p*-Si@ATO, *p*-Si and commercial Si. **d** High-rate cycling performances of *p*-Si@ATO anode at 25 °C. **e** Cycling performance of *p*-Si@ATO||LFP pouch cell without pre-lithiation at 25 °C. **f** GITT of *p*-Si@ATO, *p*-Si and commercial Si at 0.2 A g^{-1} after 10 cycles. **g-i** DRT in initial charging process for *p*-Si@ATO, *p*-Si and commercial Si electrode at 25 °C. **j** Comparison of the performances of the *p*-Si@ATO with other Si-based anode materials

cycling stability and thermal stability outperform the *p*-Si and state-of-the-art Si-base materials reported in literature (Fig. 3j and Table S3) [29, 41–45]. Meanwhile, without any additional conductive agent, *p*-Si@ATO electrode with a high loading anode of 1.8 mg cm^{-2} displays an area capacity of approximately 3.2 mAh cm^{-2} at 0.2 A g^{-1} (Fig. S17). Furthermore, *p*-Si@ATO||LFP full-cell are assembled to test *p*-Si@ATO application performance (Figs. 3e and S18), the cell without any pre-lithiation have a capacity retention of 77.4% after 50 cycles, while the average CE over 50 cycles is 97.5%.

To further elucidate the kinetics of Li^+ transport in the electrodes, the Li^+ diffusion coefficient is measured using the galvanostatic intermittent titration technique (GITT). As expected, the Li^+ diffusion rate is faster at the elevated temperature of 50 °C compared to the standard condition of 25 °C (Fig. 3f). Notably, the *p*-Si@ATO shows a faster diffusion of Li^+ compared to that of the *p*-Si and commercial Si. Specifically, during the delithiation, the diffusion coefficient of *p*-Si@ATO is about 10^{-11} cm^2 s^{-1}, two orders of magnitude higher than that of commercial Si (10^{-13} cm^2 s^{-1}). This significant difference indicates that the commercial Si suffers from slow delithiation kinetics, which adversely affects its rate performance. In contrast, the mesoporous structure and the presence of active sites on the surface of *p*-Si@ATO are conducive to the rapid

 https://doi.org/10.1007/s40820-025-01701-8

adsorption and mass transfer of the electrolyte. These characteristics are crucial in contributing to the material's outstanding high-rate performance and enhanced reversible capacity. EIS (Fig. S21) measurements further confirm the differences in the interfacial properties after the first cycle at a current density of 0.2 A g^{-1}. The impedance of *p*-Si@ATO at 25 °C is significantly lower than that of *p*-Si and commercial Si. Meanwhile, the difference in impedance between *p*-Si@ATO and commercial Si diminishes at 50 °C. This suggests that the kinetic processes of *p*-Si@ATO are superior to those of *p*-Si and commercial Si, and that there are variations in the interfacial reactions that occur at different temperatures. More specifically, DRT (Fig. 3g–i) analysis is utilized to investigate the interface evolution at initial charging process. The emergence of peaks at τ_1 below 10^{-5} s which can be ascribed to the contact impedance between the electrode material and the current collector [46]. The τ_2 peak is indicative of the SEI impedance on the lithium (Fig. S22). The τ_3 and τ_4 peaks are representative of the SEI impedance (R_{SEI}) and charge transfer impedance (R_{ct}) on Si electrode [47, 48]. The R_{ct} and R_{SEI} impedances of *p*-Si@ATO are substantially reduced compared to those of *p*-Si and commercial Si, particularly the disparity in R_{SEI} on Si electrode side associated with the τ_3 peak. During the delithiation phase between 0.1 and 0.5 V, the τ_3 and τ_4 peaks exhibit a significant lower. This suggests that the SEI constructed on the surface of *p*-Si@ATO has faster delithiation kinetics, which is advantageous for attaining high capacities and high-rate capabilities.

3.4 Interface Analysis on Electrodes

A series of analytical techniques are utilized to provide a detailed comparison of the SEI on *p*-Si@ATO and commercial Si electrodes after cycling. HRTEM images (Fig. 4a, b) reveal that after 100 cycles, the SEI on the *p*-Si@ATO is more uniform and thinner than that on commercial Si, which is beneficial for battery performance as it can provide a stable interface for Li^+ transport while minimizing resistance and protecting the electrode material. Furthermore, the integrity of the electrodes is investigated. Both types of Si anodes start with a similar initial thickness of about 10 μm (Fig. 4c, d). After 10 cycles, the *p*-Si@ATO electrode thickness increases by about 63.6%, whereas the commercial Si electrode expands by about 140.0% (Fig. 4e, f). This suggests that the porous structure of *p*-Si@ATO mitigates the volume change of Si during lithiation and delithiation processes, which helps maintain the electrode's integrity. On the other hand, the results also indicate that the *p*-Si@ATO electrode maintains a more effective SEI and suffers less mechanical degradation compared to commercial Si, which leads to better electrochemical performance and could potentially translate into longer battery life and higher stability.

Linear sweep voltammetry (LSV) shows multiple reduction peaks between 2.0 and 0.5 V during the initial discharge process at 25 °C (Fig. 4g), which are associated with the reduction and decomposition of the electrolyte that leads to SEI formation [18]. Quasi in situ XPS (Fig. 4h) further confirms the SEI formation process on the *p*-Si@ATO electrode at various discharge voltages. In F 1*s* spectra, a small LiF peak about 685 eV is observed at 2.0 V [49], which grows as the voltage is reduced to 1.5 V. In C 1*s* spectra, alongside peaks corresponding to C-O and C=O increases in intensity, which are indicative of organic SEI components [49]. A small amount of $ROCO_2Li$ is also detected. A significant increase in the C-O peak at 1.0 V corresponds to the decomposition of EC [50], which is consistent with the LSV. As the discharge continues, the electrolyte decomposition progresses, leading to more side reactions and substantial SEI formation. The LiF peak weakens, while peaks for side reaction products Li_xPF_y and $Li_xPO_yF_z$ become more prominent (Fig. S24). At 0.01 V, there is a significant increase in Li_2CO_3 content. LiF is typically formed at higher voltages (> 1.5 V) than that of Li_2CO_3 and organic SEI components, and its presence is crucial for a dense and stable inorganic SEI [4]. In situ Raman spectroscopy (Figs. 4i and S25) supports these findings, showing a peak that may correspond to LiF (416.6 cm^{-1}) at approximately 1.8 V [51, 52]. Additionally, the decrease in the intensity of the Si peak (518.0 cm^{-1}) at around 1.0 V suggests the formation of the SEI, which diminishes the Si signal [52, 53].

The SEI forms on the electrode surface during the initial charge–discharge cycles and acts as a barrier that regulates ion transport while preventing further electrolyte decomposition, which are extra unstable on the surfaces of Si. The double-layer structure of the SEI is identified as consists of an inorganic inner layer that includes species such as LiF, Li_2CO_3, Li_2O and an organic outer layer composed

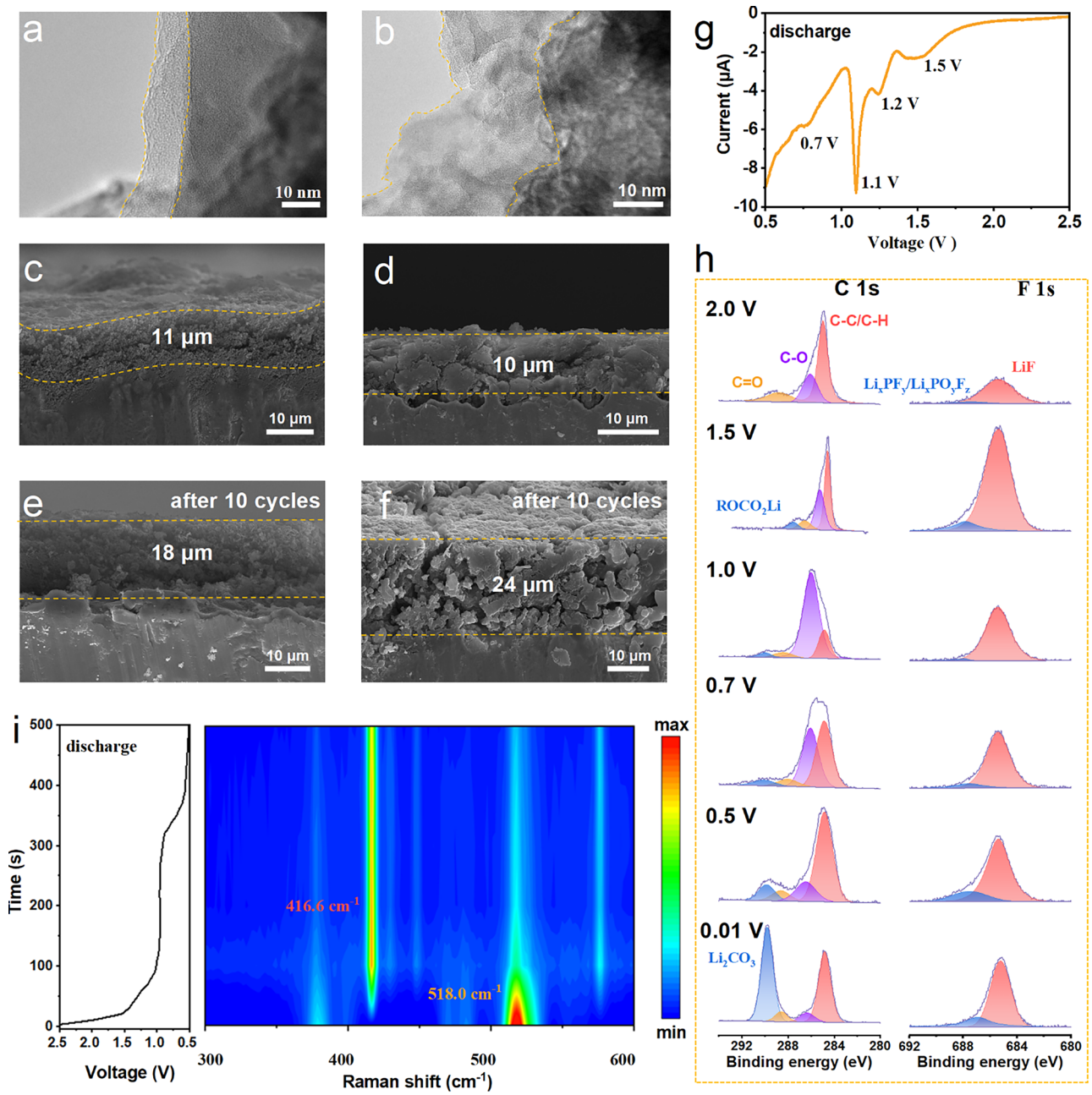

Fig. 4 Interface and electrode analysis of *p*-Si@ATO anode. **a**, **b** HRTEM images of *p*-Si@ATO **a** and commercial Si **b** electrodes after 100 cycles. **c-f** Cross-sectional SEM images of *p*-Si@ATO **c**, **d** and commercial Si **e, f** electrodes. **g** LSV in initial discharge process of *p*-Si@ATO at 0.05 mV s^{-1}. **h** Quasi in situ XPS of *p*-Si@ATO electrode at different voltages. **i** In situ Raman spectroscopy contour of *p*-Si@ATO electrode in first discharge process at 0.2 A g^{-1}

of compounds like lithium alkyl carbonates (RCO_2Li, $ROCO_2Li$) [4]. The evolution of the SEI over the course of cycling is investigated by performing XPS on electrodes after 1, 50, and 100 cycles. The spectrums of *p*-Si@ATO and commercial Si electrodes at 25 °C after these various cycle numbers are compared. For *p*-Si@ATO, the F 1*s* spectra (Fig. 5a) reveal an increase in the relative content of LiF with cycling, from 90.6 at% initially, to 92.1 at%, and then to 93.1 at% (Fig. S26). This trend suggests a stable and possibly thickening SEI layer. In contrast, the relative content of

https://doi.org/10.1007/s40820-025-01701-8

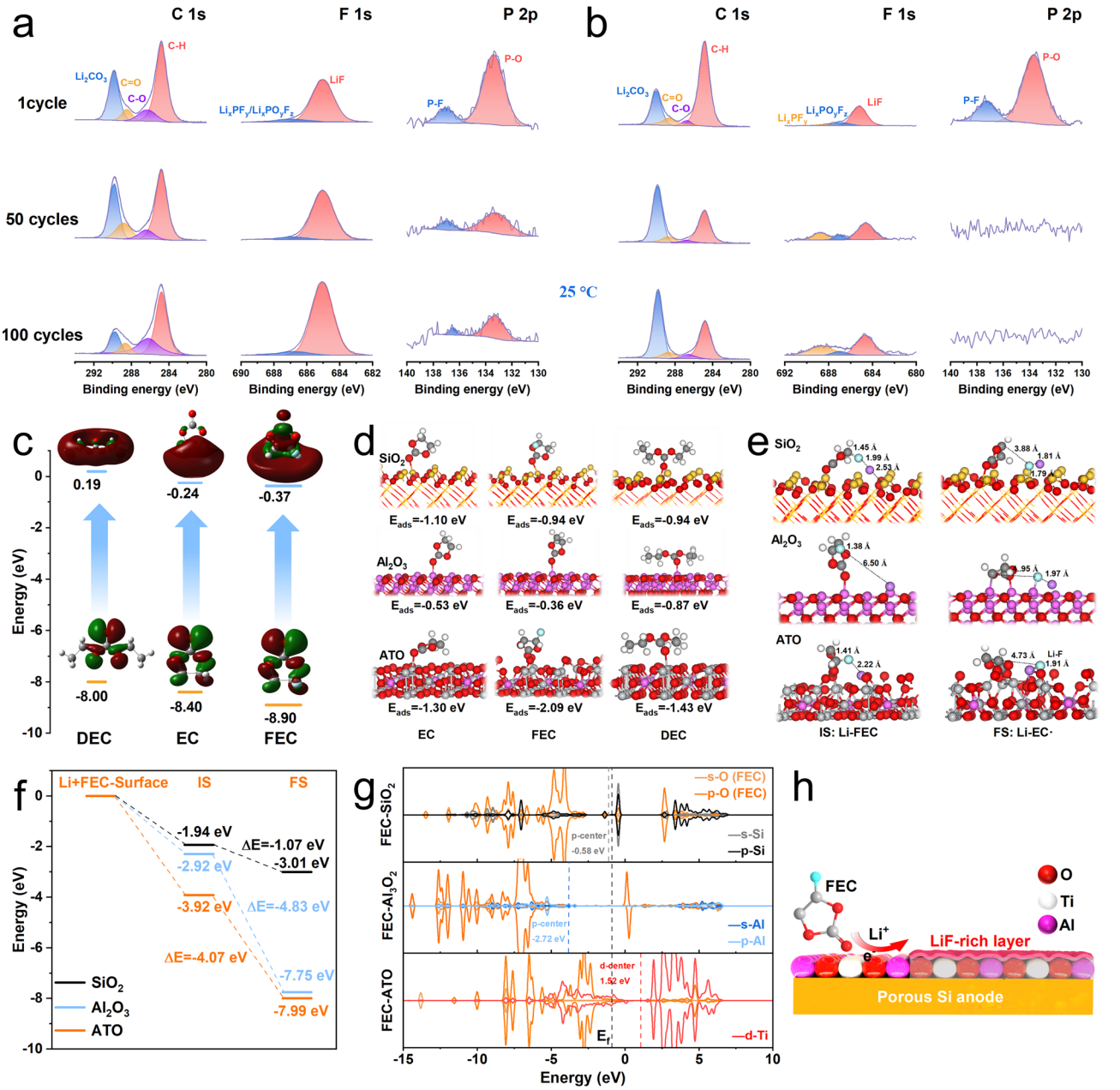

Fig. 5 **a, b** C 1*s*, F 1*s* and P 2*p* spectra of *p*-Si@ATO (**a**) and commercial Si (**b**) at 25 °C. All spectra were measured using disassembled half-cell electrodes at 100% SOC. **c** Electronic transition and related E_{gap} of solvent molecules. **d** Adsorption configurations of solvent molecules on the different surfaces. **e, f** LiF forming structure and the relative energy profile over the SiO_2, Al_2O_3 and ATO surfaces. **g** PDOS with FEC on SiO_2, Al_2O_3 and ATO surfaces. **h** Schematic illustration of interfacial catalysis about the formation of LiF with FEC solvent over ATO

LiF on commercial Si electrodes show a decrease from 79.3 to 63.9 at% and further to 54.5 at%, which might indicate a fragile SEI that is breaking down or undergoing continuous reconstruction. This instability can lead to excessive consumption of the electrolyte, gas generation, and the formation of a porous and weak mechanical SEI. LiF is particularly desirable in the SEI due to its electronic insulation properties and mechanical stability, which are beneficial for battery performance and durability. Doping LiF into bulk Si has also been shown to prevent the formation of the crystalline $Li_{15}Si_4$

phase, which can reduce the capacity loss [54]. It is worth noting higher relative contents of phosphate-containing species ($Li_xPO_yF_z$ at 687.0 eV and Li_xPF_y at 688.5 eV) on the commercial Si compared to that on the *p*-Si@ATO [49]. These species are often associated with side reactions on the electrode surface, suggesting that commercial Si experiences more severe side reactions that can degrade battery performance over time.

The C 1*s* spectra (Fig. 5a) analysis provides insights into the carbon-containing components of the SEI. For the *p*-Si@ATO electrodes, the relative content of Li_2CO_3 at 289.8 eV [49] initially rises and then falls as the number of cycle increases, suggesting formation of Li_2CO_3 after a reaction when the electrolyte decomposes, which is part of inorganic layer of SEI, followed by a decomposition of part of Li_2CO_3 gradually in the following cycles. The situation with commercial Si is totally different, where, the relative content of Li_2CO_3 keeps increasing (Fig. 5b), which could be due to ongoing breakdown and reconstruction of the SEI. The continuous reaction between Li_2CO_3 and the electrolyte can produce gases, contributing to a loose SEI [55]. The repeating construction of SEI exacerbate electrolyte decomposition and would lead to limited battery performance and life. The P element relates to the decomposition of the electrolyte component $LiPF_6$. In the F 1*s* spectrum, decomposition products such as Li_xPF_y and $Li_xPO_yF_z$ are detected (Fig. 5b). However, for the commercial Si electrode, P-O bond (133.4 eV) and P-F bond (137.0 eV) signals are weak after the first cycle [56], due probably to a consumption of the electrolyte that leads to a thick organic SEI layer which could obscure the P signals from the XPS measurement. In contrast, the *p*-Si@ATO electrode (Fig. 5a) still shows well-visible P signals even after 100 cycles, indicating a thinner SEI which is a clear indication of less electrolyte consumption and fewer side reactions (Li_2CO_3 and organic SEI). In summary, the results suggest that the SEI on the *p*-Si@ATO electrode is better composed with a higher content of LiF and fewer side reaction products. Owing to dense LiF layer and better interface, the SEI on *p*-Si@ATO demonstrates higher stability. The improved SEI structure on *p*-Si@ATO provides enhanced protection against side reactions, contributing to its superior cycling stability and capacity retention compared to commercial Si.

To further elucidate the compositional characteristics and distinctions of the SEI formed on the three silicon-based electrodes, time-of-flight secondary ion mass spectrometry (ToF–SIMS) depth profiling analysis was systematically performed. The corresponding results are presented in Fig. S27. The acquired depth profiles reveal critical insights into the spatial distribution and temporal evolution trends of key ionic species. Specifically, characteristic secondary ions including Si^- (representative of Si), $C_2H_2O^-$ (indicative of organic constituents), LiF_2^- (associated with LiF) and $LiCO_3^-$ (corresponding to Li_2CO_3) are monitored as functions of sputtering time. As evidenced by Fig. S27c, the Si^- signal in the commercial Si electrode emerges only after 100 s of ion etching, accompanied by a continuous attenuation of organic-related signals ($C_2H_2O^-$). This observation implies the presence of a relatively thick organic-dominated SEI layer at the surface, with progressively increasing Li_2CO_3 content and limited LiF accumulation. In contrast, both *p*-Si and *p*-Si@ATO electrodes exhibit earlier emergence of Si^- signals during the etching process. Notably, the *p*-Si@ATO electrode demonstrates substantial LiF enrichment coupled with markedly reduced $C_2H_2O^-$ content within the SEI. These findings collectively suggest that the *p*-Si@ATO electrode possesses the thinnest SEI layer among the investigated systems, featuring a distinctive architecture comprising a sparse outer organic layer and a dense inorganic-rich interfacial region predominantly composed of LiF, which exhibits an intensified concentration.

3.5 Theoretical Calculation

The interfacial catalytic mechanisms of ATO are verified by DFT calculation. Typically, solvents possessing low LUMO values would undergo prior reduction at the surface to dictate the inner SEI components [57]. FEC manifests the lowest LUMO value, − 0.37 eV, indicative of its preferential decomposition during initial lithiation (Fig. 5c). The three solvent adsorptions are performed over the periodic models of SiO_2, Al_2O_3 and ATO. The adsorption energy of these solvent molecules over the surface of ATO is lower than that of the SiO_2 and Al_2O_3 (Fig. 5d), demonstrating superior adsorption of ATO surface. Notably, the lower adsorption energy of the FEC on ATO (− 2.09 eV) imply that FEC is more easily be accumulated on the surface of ATO. The intermediate optimization of decomposed product LiF's initial state (IS) and final state (FS) with FEC solvent is performed (Fig. 5e). For the IS, the C-F bond in FEC is

 https://doi.org/10.1007/s40820-025-01701-8

about 1.45 and 1.41 Å, respectively, on the surface of SiO_2 and ATO. In comparison, the C-F bond of FEC on the Al_2O_3 resulted in the shortest bond length (1.38 Å) due to the far distance of active Al on the surface. Considering FS structural optimizations, after forming Li-F, the C-F bond over three surface models is 3.88–4.95 Å. Longer C-F bonds indicate that it is more likely to break and form LiF [25]. The relative energy diagram of IS and FS on SiO_2, Al_2O_3 and ATO is shown in Fig. 5f. Subsequent to the genesis of Li-F, the energy of the ATO in FS is − 7.99 eV, which is lower than that of the Al_2O_3 (− 7.75 eV), and considerably lower that of SiO_2 (− 3.01 eV). In comparison, the energy profile of LiF with FEC solvent over the ATO surface resulted in more exothermic intermediate energies.

Furthermore, the electronic properties of SiO_2, Al_2O_3, and ATO with the FEC molecule are theoretically investigated using the partial density of state (PDOS, Fig. 5g). In general, shifting the *p*-band or *d*-band centers of active sites is an effective way to regulate electronic and geometric structures because downshifting can aid the desorption of active intermediates [58]. Meanwhile, the upshifting promotes the active intermediates' adsorption, enhancing the active sites' reactivity, which significantly facilitates the activity catalyst's surfaces. The ATO shows the *d*-center at 1.52 eV, crosses the Femi-energy level, which suggests a more active surface in comparison to the SiO_2 and Al_2O_3, where the *p*-center positioned at − 0.58 and − 2.72 eV, respectively. The FEC adsorption on the catalysts resulted in the upshift PDOS in both the *p*-band and *d*-band, as seen in the values of the *p*-center and *d*-center (Fig. S28). The adsorption strength of FEC on ATO is more significant, confirming that FEC is most likely to be decomposed to LiF on the ATO surface, which is an important factor in the perdurable cycling stability of the *p*-Si@ATO electrode (Fig. 5h).

The "molecular concentration-in situ conversion" mechanisms of the functional interface on mesoporous Si microsphere can be described (Fig. 1). Initially, the solvent molecules are adsorbed on the electrode surface, similar with supercapacitor, which are accumulated on the surfaces. Enrich of the FEC is then directly catalyzed to the LiF-rich SEI. Compared with commercial Si, the *p*-Si@ATO proved to with lower adsorption energy with FEC. Moreover, the LiF-rich SEI derived from ultra-thin oxide layer reduces the resistance of mass transfer, which is conducive to improving the high-rate performance. As the synergetic effect of the both molecular concentration and in situ conversion of functional interface, the *p*-Si@ATO is proved to own LiF-rich robust and thinner inorganic SEI layer than other Si-based materials. The high-rate and high temperature stabilities of *p*-Si@ATO are facilitated by the effective resolution of electrolyte depletion at the surface functional interface, while the mesopore structure of the microsphere acts as a buffer, safeguarding against cracking and preserving electrode integrity.

4 Conclusion

In this work, an ultra-thin catalytic interface on mesoporous Si has been innovatively developed through an in situ etching and co-growth process. Stemming from the catalytic effect of defect-rich interface, and the concentrated accumulation of FEC within the mesopores, a uniform LiF-rich robust SEI would be formed. The as-protected mesoporous Si microsphere has highly reversible capacity at high current density 25 A g^{-1} (692 mAh g^{-1} at 25 °C and 270 mAh g^{-1} at 50 °C) and high-temperature capacity retention (80.0%) over 500 cycles at 2 A g^{-1}. Particularly, this Si anode performs long cycling stability as long as 1000 cycles even at an elevated current density of 20 A g^{-1}. Consequently, this strategy points out the effective way to mitigate capacity degradation in Si, particularly at harsh condition, satisfying the critical requirement for a high safety and long durable anode with both high energy density and high power density.

Acknowledgements The authors acknowledge the National Key R&D Plan of the Ministry of Science and Technology of China (2022YFE0122400), National Natural Science Foundation of China (52002238, 22102207), Science and Technology Commission of Shanghai Municipality (22ZR1423800, 21ZR1465200, 23ZR1423600), Shanghai Municipal Education Commission and the NSRF via the Program Management Unit for Human Resources & Institutional Development, Research and Innovation (B49G680115). The XAS measurement was carried out with the support of Shanghai Synchrotron Radiation Facility, the beamline BL14W1.

Authors' Contributions Z.H. and P.M. contributed equally to this work. Y.L. conceived the ideas. Z.H. prepared samples and carried out the experiments with suggestions from Y.L. and drafted the manuscript under the direction of Y.L. P.M., N.Y. and S.J. provided DFT calculations and drafted the text of the DFT part. B.Z., H.M. and K.L. helped with collection of the characterization data. Y.H., Y.W. and L.L. offered advice during the experiment. L.S., S.Y. provided the platform and the funding support. Z.H and Y.L organized the final manuscript according to all the authors.

Declarations

Conflict of Interest The authors declare no interest conflict. They have no known competing financial interests or personal relationships that could have appeared to influence the work reported in this paper.

Supplementary Information The online version contains supplementary material available at https://doi.org/10.1007/s40820-025-01701-8.

References

1. Y. He, L. Jiang, T. Chen, Y. Xu, H. Jia et al., Progressive growth of the solid-electrolyte interphase towards the Si anode interior causes capacity fading. Nat. Nanotechnol. **16**, 1113–1120 (2021). https://doi.org/10.1038/s41565-021-00947-8
2. N. Kim, Y. Kim, J. Sung, J. Cho, Issues impeding the commercialization of laboratory innovations for energy-dense Si-containing lithium-ion batteries. Nat. Energy **8**, 921–933 (2023). https://doi.org/10.1038/s41560-023-01333-5
3. S. Malmgren, K. Ciosek, M. Hahlin, T. Gustafsson, M. Gorgoi et al., Comparing anode and cathode electrode/electrolyte interface composition and morphology using soft and hard X-ray photoelectron spectroscopy. Electrochim. Acta **97**, 23–32 (2013). https://doi.org/10.1016/j.electacta.2013.03.010
4. B. Jagger, M. Pasta, Solid electrolyte interphases in lithium metal batteries. Joule **7**, 2228–2244 (2023). https://doi.org/10.1016/j.joule.2023.08.007
5. R. Yu, Y. Pan, Y. Jiang, L. Zhou, D. Zhao et al., Regulating lithium transfer pathway to avoid capacity fading of nano Si through sub-nano scale interfused SiO_x/C coating. Adv. Mater. **35**, 2306504 (2023). https://doi.org/10.1002/adma.202306504
6. X.-B. Cheng, S.-J. Yang, Z. Liu, J.-X. Guo, F.-N. Jiang et al., Electrochemically and thermally stable inorganics-rich solid electrolyte interphase for robust lithium metal batteries. Adv. Mater. **36**, e2307370 (2024). https://doi.org/10.1002/adma.202307370
7. S.-J. Yang, N. Yao, F.-N. Jiang, J. Xie, S.-Y. Sun et al., Thermally stable polymer-rich solid electrolyte interphase for safe lithium metal pouch cells. Angew. Chem. Int. Ed. **61**, e202214545 (2022). https://doi.org/10.1002/anie.202214545
8. Y. Li, M. Liu, X. Feng, Y. Li, F. Wu et al., How can the electrode influence the formation of the solid electrolyte interface? ACS Energy Lett. **6**, 3307–3320 (2021). https://doi.org/10.1021/acsenergylett.1c01359
9. H. Wei, G. Qu, X. Zhang, B. Ren, S. Li et al., Boosting aqueous non-flow zinc–bromine batteries with a two-dimensional metal–organic framework host: an adsorption-catalysis approach. Energy Environ. Sci. **16**, 4073–4083 (2023). https://doi.org/10.1039/D3EE01639K
10. H. Fan, X.-W. Gao, H. Xu, Y. Ding, S.-X. Dou et al., Catalytic effect in lithium metal batteries: From heterogeneous catalyst to homogenous catalyst. J. Energy Chem. **90**, 305–326 (2024). https://doi.org/10.1016/j.jechem.2023.11.025
11. P. Liang, S. Di, Y. Zhu, Z. Li, S. Wang et al., Realization of long-life proton battery by layer intercalatable electrolyte. Angew. Chem. Int. Ed. **63**, e202409871 (2024). https://doi.org/10.1002/anie.202409871
12. C.M. Efaw, Q. Wu, N. Gao, Y. Zhang, H. Zhu et al., Localized high-concentration electrolytes get more localized through micelle-like structures. Nat. Mater. **22**, 1531–1539 (2023). https://doi.org/10.1038/s41563-023-01700-3
13. Y.S. Meng, V. Srinivasan, K. Xu, Designing better electrolytes. Science **378**, eabq3750 (2022). https://doi.org/10.1126/science.abq3750
14. T. Jaumann, J. Balach, U. Langklotz, V. Sauchuk, M. Fritsch et al., Lifetime vs. rate capability: Understanding the role of FEC and VC in high-energy Li-ion batteries with nano-silicon anodes. Energy Storage Mater. **6**, 26–35 (2017). https://doi.org/10.1016/j.ensm.2016.08.002
15. Y. Jin, N.H. Kneusels, L.E. Marbella, E. Castillo-Martínez, P.C.M.M. Magusin et al., Understanding fluoroethylene carbonate and vinylene carbonate based electrolytes for Si anodes in lithium ion batteries with NMR spectroscopy. J. Am. Chem. Soc. **140**, 9854–9867 (2018). https://doi.org/10.1021/jacs.8b03408
16. J. Chen, X. Fan, Q. Li, H. Yang, M.R. Khoshi et al., Electrolyte design for LiF-rich solid–electrolyte interfaces to enable high-performance microsized alloy anodes for batteries. Nat. Energy **5**, 386–397 (2020). https://doi.org/10.1038/s41560-020-0601-1
17. M. Tian, Z. Jin, Z. Song, R. Qiao, Y. Yan et al., Domino reactions enabling sulfur-mediated gradient interphases for high-energy lithium batteries. J. Am. Chem. Soc. **145**, 21600–21611 (2023). https://doi.org/10.1021/jacs.3c07908
18. S.J. An, J. Li, C. Daniel, D. Mohanty, S. Nagpure et al., The state of understanding of the lithium-ion-battery graphite solid electrolyte interphase (SEI) and its relationship to formation cycling. Carbon **105**, 52–76 (2016). https://doi.org/10.1016/j.carbon.2016.04.008
19. B. Han, Y. Zou, G. Xu, S. Hu, Y. Kang et al., Additive stabilization of SEI on graphite observed using cryo-electron microscopy. Energy Environ. Sci. **14**, 4882–4889 (2021). https://doi.org/10.1039/d1ee01678d

20. H. Wan, J. Xu, C. Wang, Designing electrolytes and interphases for high-energy lithium batteries. Nat. Rev. Chem. **8**, 30–44 (2024). https://doi.org/10.1038/s41570-023-00557-z
21. J. Wang, Z. Yang, B. Mao, Y. Wang, Y. Jiang et al., Transgenic engineering on silicon surfaces enables robust interface chemistry. ACS Energy Lett. **7**, 2781–2791 (2022). https://doi.org/10.1021/acsenergylett.2c01202
22. S. Tan, Z. Shadike, J. Li, X. Wang, Y. Yang et al., Additive engineering for robust interphases to stabilize high-Ni layered structures at ultra-high voltage of 4.8 V. Nat. Energy **7**, 484–494 (2022). https://doi.org/10.1038/s41560-022-01020-x
23. M. Liu, F. Wu, Y. Gong, Y. Li, Y. Li et al., Interfacial-catalysis-enabled layered and inorganic-rich SEI on hard carbon anodes in ester electrolytes for sodium-ion batteries. Adv. Mater. **35**, e2300002 (2023). https://doi.org/10.1002/adma.202300002
24. Z. Lu, J. Wang, W. Feng, X. Yin, X. Feng et al., Zinc single-atom-regulated hard carbons for high-rate and low-temperature sodium-ion batteries. Adv. Mater. **35**, 2211461 (2023). https://doi.org/10.1002/adma.202211461
25. J. Ge, C. Ma, Y. Wan, G. Tang, H. Dai et al., Electrocatalysis of Fe-N-C bonds driving reliable interphase and fast kinetics for phosphorus anode in sodium-ion batteries. Adv. Funct. Mater. **33**, 2305803 (2023). https://doi.org/10.1002/adfm.202305803
26. C. Yan, H.-R. Li, X. Chen, X.-Q. Zhang, X.-B. Cheng et al., Regulating the inner Helmholtz plane for stable solid electrolyte interphase on lithium metal anodes. J. Am. Chem. Soc. **141**, 9422–9429 (2019). https://doi.org/10.1021/jacs.9b05029
27. S. Mao, J. Mao, Z. Shen, Q. Wu, S. Zhang et al., Specific adsorption-oxidation strategy in cathode inner Helmholtz plane enabling 4.6 V practical lithium-ion full cells. Nano Lett. **23**, 7014–7022 (2023). https://doi.org/10.1021/acs.nanolett.3c01700
28. Y. Wang, H. Li, S. Di, B. Zhai, P. Niu et al., Constructing long-cycling crystalline C_3N_4-based carbonaceous anodes for sodium-ion battery *via* N configuration control. Carbon Energy **6**, e388 (2024). https://doi.org/10.1002/cey2.388
29. Y.-F. Tian, S.-J. Tan, C. Yang, Y.-M. Zhao, D.-X. Xu et al., Tailoring chemical composition of solid electrolyte interphase by selective dissolution for long-life micron-sized silicon anode. Nat. Commun. **14**, 7247 (2023). https://doi.org/10.1038/s41467-023-43093-6
30. X. Liu, J. Liu, L. Li, R. Guo, X. Zhang et al., Hydrodesulfurization of dibenzothiophene on TiO_{2-x}-modified Fe-based catalysts: electron transfer behavior between TiO_{2-x} and Fe species. ACS Catal. **10**, 9019–9033 (2020). https://doi.org/10.1021/acscatal.0c01068
31. X. Hu, J. Song, S. Zheng, Z. Sun, C. Li, Insight into the defective sites of TiO_2/sepiolite composite on formaldehyde removal and H_2 evolution. Mater. Today Energy **24**, 100932 (2022). https://doi.org/10.1016/j.mtener.2021.100932
32. W. Wang, C.-H. Lu, Y.-R. Ni, J.-B. Song, M.-X. Su et al., Enhanced visible-light photoactivity of {001}facets dominated TiO_2 nanosheets with even distributed bulk oxygen vacancy and Ti^{3+}. Catal. Commun. **22**, 19–23 (2012). https://doi.org/10.1016/j.catcom.2012.02.011
33. H. Zhang, L. Wu, R. Feng, S. Wang, C.-S. Hsu et al., Oxygen vacancies unfold the catalytic potential of NiFe-layered double hydroxides by promoting their electronic transport for oxygen evolution reaction. ACS Catal. **13**, 6000–6012 (2023). https://doi.org/10.1021/acscatal.2c05783
34. Y. Tang, Y. Zhang, O.I. Malyi, N. Bucher, H. Xia et al., Identifying the origin and contribution of surface storage in TiO_2(B) nanotube electrode by *in situ* dynamic valence state monitoring. Adv. Mater. **30**, 1802200 (2018). https://doi.org/10.1002/adma.201802200
35. Y. Jiang, D. Baimanov, S. Jin, J. Cheuk-Fung Law, P. Zhao et al., *In situ* turning defects of exfoliated Ti_3C_2 MXene into Fenton-like catalytic active sites. Proc. Natl. Acad. Sci. U.S.A. **120**, e2210211120 (2023). https://doi.org/10.1073/pnas.2210211120
36. W. Yoon, S. Lee, Y. Noh, S. Park, Y. Kim et al., Highly selective catalytic dechlorination of dichloromethane to chloromethane over Al−Ti mixed oxide catalysts. ChemCatChem **12**, 5098–5108 (2020). https://doi.org/10.1002/cctc.202000879
37. J. Cheng, J. Xie, Y. Xi, X. Wu, R. Zhang et al., Selective upcycling of polyethylene terephthalate towards high-valued oxygenated chemical methyl p-methyl benzoate using a Cu/ZrO_2 catalyst. Angew. Chem. Int. Ed. **63**, e202319896 (2024). https://doi.org/10.1002/anie.202319896
38. P. Sudarsanam, H. Li, T.V. Sagar, TiO_2-based water-tolerant acid catalysis for biomass-based fuels and chemicals. ACS Catal. **10**, 9555–9584 (2020). https://doi.org/10.1021/acscatal.0c01680
39. K.S. Han, M.-S. Lee, N. Kim, D. Choi, S. Chae et al., Lithium-ion hopping weakens thermal stability of $LiPF_6$ carbonate electrolytes. Cell Rep. Phys. Sci. **5**, 101768 (2024). https://doi.org/10.1016/j.xcrp.2023.101768
40. L. Lv, Y. Wang, W. Huang, Y. Wang, X. Li et al., Mechanism study on the cycling stability of silicon-based lithium ion batteries as a function of temperature. Electrochim. Acta **437**, 141518 (2023). https://doi.org/10.1016/j.electacta.2022.141518
41. D. Wang, Y. Ma, W. Xu, S. Zhang, B. Wang et al., Controlled isotropic canalization of microsized silicon enabling stable high-rate and high-loading lithium storage. Adv. Mater. **35**, e2212157 (2023). https://doi.org/10.1002/adma.202212157
42. X. Zhang, D. Wang, X. Qiu, Y. Ma, D. Kong et al., Stable high-capacity and high-rate silicon-based lithium battery anodes upon two-dimensional covalent encapsulation. Nat. Commun. **11**, 3826 (2020). https://doi.org/10.1038/s41467-020-17686-4
43. W. An, B. Gao, S. Mei, B. Xiang, J. Fu et al., Scalable synthesis of ant-nest-like bulk porous silicon for high-performance lithium-ion battery anodes. Nat. Commun. **10**, 1447 (2019). https://doi.org/10.1038/s41467-019-09510-5
44. A.-M. Li, Z. Wang, T.P. Pollard, W. Zhang, S. Tan et al., High voltage electrolytes for lithium-ion batteries with micro-sized

silicon anodes. Nat. Commun. **15**, 1206 (2024). https://doi.org/10.1038/s41467-024-45374-0

45. Q. Wang, M. Zhu, G. Chen, N. Dudko, Y. Li et al., High-performance microsized Si anodes for lithium-ion batteries: insights into the polymer configuration conversion mechanism. Adv. Mater. **34**, e2109658 (2022). https://doi.org/10.1002/adma.202109658
46. X. Chen, L. Li, M. Liu, T. Huang, A. Yu, Detection of lithium plating in lithium-ion batteries by distribution of relaxation times. J. Power Sources **496**, 229867 (2021). https://doi.org/10.1016/j.jpowsour.2021.229867
47. K. Pan, F. Zou, M. Canova, Y. Zhu, J.-H. Kim, Comprehensive electrochemical impedance spectroscopy study of Si-based anodes using distribution of relaxation times analysis. J. Power Sources **479**, 229083 (2020). https://doi.org/10.1016/j.jpowsour.2020.229083
48. Y. Qian, Y. Liang, W. Zhang, B. Xi, N. Lin, Thermal polymerization of ion-modified carbon dots into multi-functional LiF-carbon interface for stabilizing SiO anode. Energy Storage Mater. **63**, 102996 (2023). https://doi.org/10.1016/j.ensm.2023.102996
49. P. Mu, S. Zhang, H. Zhang, J. Li, Z. Liu et al., A spidroin-inspired hierarchical-structure binder achieves highly integrated silicon-based electrodes. Adv. Mater. **35**, 2303312 (2023). https://doi.org/10.1002/adma.202303312
50. L. Wang, A. Menakath, F. Han, Y. Wang, P.Y. Zavalij et al., Identifying the components of the solid–electrolyte interphase in Li-ion batteries. Nat. Chem. **11**, 789–796 (2019). https://doi.org/10.1038/s41557-019-0304-z
51. C.-Y. Li, Y. Yu, C. Wang, Y. Zhang, S.-Y. Zheng et al., Surface changes of $LiNi_xMn_yCo_{1-x-y}O_2$ in Li-ion batteries using *in situ* surface-enhanced Raman spectroscopy. J. Phys. Chem. C **124**, 4024–4031 (2020). https://doi.org/10.1021/acs.jpcc.9b11677
52. A. Krause, O. Tkacheva, A. Omar, U. Langklotz, L. Giebeler et al., *In situ* Raman spectroscopy on silicon nanowire anodes integrated in lithium ion batteries. J. Electrochem. Soc. **166**, A5378–A5385 (2019). https://doi.org/10.1149/2.0541903jes
53. S. Mei, B. Xiang, S. Guo, J. Deng, J. Fu et al., Design and electrochemical mechanism of the MgF_2 coating as a highly stable and conductive interlayer on the Si anode for high-performance Li-ion batteries. Adv. Funct. Mater. **34**, 2301217 (2024). https://doi.org/10.1002/adfm.202301217
54. Y. Li, Z. Cao, Y. Wang, L. Lv, J. Sun et al., New insight into the role of fluoro-ethylene carbonate in suppressing Li-trapping for Si anodes in lithium-ion batteries. ACS Energy Lett. **8**, 4193–4203 (2023). https://doi.org/10.1021/acsenergylett.3c01328
55. B. Han, Z. Zhang, Y. Zou, K. Xu, G. Xu et al., Poor stability of Li_2CO_3 in the solid electrolyte interphase of a lithium-metal anode revealed by cryo-electron microscopy. Adv. Mater. **33**, 2100404 (2021). https://doi.org/10.1002/adma.202100404
56. W. Huang, Y. Wang, L. Lv, Y. Wang, X. Li et al., *In situ* construction of a multifunctional interface regulator with amino-modified conjugated diene toward high-rate and long-cycle silicon anodes. ACS Appl. Mater. Interfaces **14**, 13317–13325 (2022). https://doi.org/10.1021/acsami.1c24578
57. J. Huang, X. Guo, X. Du, X. Lin, J.-Q. Huang et al., Nanostructures of solid electrolyte interphases and their consequences for microsized Sn anodes in sodium ion batteries. Energy Environ. Sci. **12**, 1550–1557 (2019). https://doi.org/10.1039/C8EE03632B
58. H. Liu, X. Cai, X. Zhi, S. Di, B. Zhai et al., An amorphous anode for proton battery. Nano-Micro Lett. **15**, 24 (2022). https://doi.org/10.1007/s40820-022-00987-2

 https://doi.org/10.1007/s40820-025-01701-8